

# A Sustainable and Regenerative Process for the Treatment of Textile Effluents Using Nonphotocatalytic Water Splitting by Nanoporous Oxygen-Deficient Ferrite

Abha Shukla, Jyoti Shah, Sunidhi Badola, Tuhin K. Mandal, Ved V. Agrawal, Asit Patra, Lalsiemlien Pulamte, and Ravinder K. Kotnala\*



Cite This: *ACS Omega* 2024, 9, 8490–8502



Read Online

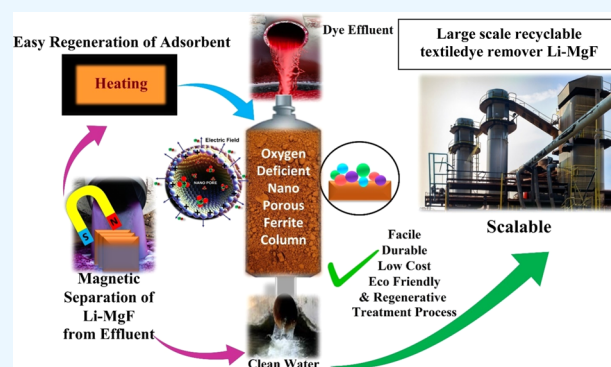
ACCESS |

Metrics & More

Article Recommendations

Supporting Information

**ABSTRACT:** Water is crucial for life. Being the world's third-largest industry, the textile industry pollutes 93 billion cubic meters of water each year. Only 28% of textile wastewater is treated by lower- to middle-income countries due to the costly treatment methods. The present work demonstrates the utilization of surface oxygen defects and nanopores in  $\text{Mg}_{0.8}\text{Li}_{0.2}\text{Fe}_2\text{O}_4$  (Li-MgF) to treat textile effluents by a highly economical, scalable, and eco-friendly process. Nanoporous, oxygen-deficient Li-MgF splits water by a nonphotocatalytic process at room temperature to produce green electricity as hydroelectric cell. The adsorbent Li-MgF can be easily regenerated by heat treatment. A 70–90% reduction in the UV absorption intensity of adsorbent-treated textile effluents was observed by UV–visible spectroscopy. The oxygen defects on Li-MgF surface and nanopores were confirmed by X-ray photoelectron spectroscopy and Brunauer–Emmett–Teller (BET) measurements, respectively. To analyze the adsorption mechanism, three known organic water-soluble dyes, brilliant green, crystal violet, and congo red, were treated with nanoporous Li-MgF. The dye decolorization efficiency of Li-MgF was recorded to be 99.84, 99.27, and 99.31% at 250  $\mu\text{M}$  concentrations of brilliant green, congo red, and crystal violet, respectively. The results of Fourier transform infrared (FTIR) spectroscopy confirmed the presence of dyes on the material surface attached through hydroxyl groups generated by water splitting on the surface of the material. Total organic carbon analysis confirmed the removal of organic carbon from the dye solutions by 82.8, 77.0, and 46.5% for brilliant green, Congo red, and crystal violet, respectively. Based on the kinetic and isotherm models, the presence of a large number of surface hydroxyl groups on the surface of the material and  $\text{OH}^-$  ions in solutions generated by water splitting was found to be responsible for the complete decolorization of all of the dyes. Adsorption of chemically diverse dyes by the nanoporous, eco-friendly, ferromagnetic, economic, and reusable Li-MgF provides a sustainable and easy way to treat textile industry effluents in large amounts.



## 1. INTRODUCTION

Dyes are the basic ingredients of the textile, food, paper, printing, product manufacturing, and processing industries.<sup>1,2</sup> Such industries in fact leave behind poison in the form of untreated wastewater worldwide, which is severely affecting the environment and life. Among them, the textile industry is a major contributor to highly colored wastewater. According to a recent study, around  $7 \times 10^7$  tons of dye is synthesized globally, and 10,000 tons of it is utilized by the textile industry alone;<sup>3</sup> globally, an estimated 2,80,000 tons of textile dyes are discharged annually as wastewater from this industry.<sup>4</sup> This industry is responsible for polluting 20% of the global clean water.<sup>5</sup> After China, India is the second largest producer and exporter of textile dyes, followed by the United States, Brazil, the United Kingdom, and Germany. India consumes around 80% of its production due to high demand in the sector.<sup>6</sup> It is expected that with the growing population, the demand for

synthetic textile dyes will further increase globally. However, the xenotoxins from organic dyes are of great concern due to their silent and easy entry into the food chain through water bodies. Most of them are carcinogenic and present a serious threat to human beings. In reality, the wastewater not only contains a variety of dyes but other pollutants such as suspended solids, toxic metals, free ammonia, chlorine, oil, grease, phosphates, carbonates, nitrates salts, and many other organic and inorganic components.<sup>7</sup> These toxic dyes have

**Received:** December 7, 2023

**Revised:** January 16, 2024

**Accepted:** January 19, 2024

**Published:** February 7, 2024



adverse impacts on human beings and the flora and fauna that come in contact with them through water, soil, or the food chain.<sup>8–10</sup> There is a wide variety of dyes based on their structure, group, and chemistry, and they differ in their levels of toxicity.<sup>11–14</sup> Such dyes not only cause toxicity but also reduce the penetration of sunlight into water due to their intense colors, resulting in decreased photosynthesis and consequently dissolved oxygen, which is crucial for aquatic life.<sup>15,16</sup>

In some countries, due to strict environmental legislations, industries are required to treat such dye-polluted wastewater before disposal into water bodies.<sup>17,18</sup> The biodegradation of these dyes has been explored as a remedial measure for several decades, but it is a very sluggish process and has not been successful at a commercial scale. Second, the process does not ensure the complete removal of toxicants. It may be completely detoxified or may be converted to less harmful secondary metabolite.<sup>19,20</sup> To date, researchers have reported many materials as adsorbents or photocatalysts for the remediation of dyes. Most of the materials reported for the degradation of dyes are based on photocatalytic degradation, in which the dye dissociates into smaller fragments.<sup>21</sup> Further, modification of these materials for more efficient degradation employs expensive compounds or metals, which make their application uneconomical, especially at a large scale. The main drawback of photocatalytic degradation is that the fragmented molecule still persists and cannot be recovered. They may have reduced toxicity, but due to their persistence in the environment, their eco-hazard and bioaccumulation cannot be overlooked. However, some studies have reported close to or complete mineralization of dyes by the photocatalytic process,<sup>22–24</sup> but the viability of the photocatalytic process on a large scale is impractical. The commercially viable adsorbent should be inexpensive, nontoxic, efficient, recoverable, and reusable.

Ferrites have been used for a wide variety of applications, such as separation of magnetic materials, humidity sensing, green and clean energy, and hydrogen generation. Besides, ferrites have also been explored for toxic dye adsorption and their removal from the wastewater. They are preferred adsorbents for toxic pollutants because they are easier and cheaper to synthesize as environmentally friendly ceramic materials, and most importantly, their magnetic nature helps in the easy separation of adsorbents from water bodies.<sup>25–27</sup> The most recent revolutionary application of ferrites is in the meticulously engineered hydroelectric cell invention based on water splitting via a nonphotocatalytic process through oxygen vacancies and nanopores created in the ferrite.<sup>28</sup> The hydroelectric cell device generates green electricity along with zinc hydroxide nanoparticles and hydrogen, in turn, as cell byproducts using a few drops of water only.<sup>29,30</sup> In the present work, a new dimension has been added to the nanoporous, oxygen-deficient Li-MgF by an inexpensive, scalable method to explore the adsorption of dyes in textile wastewater. So far, very few studies have been reported on the defect-mediated adsorption of dyes.<sup>31,32</sup> The results are very encouraging as the study reveals that Li-MgF is able to decolorize a wide variety of dyes, such as dyes from triarylmethane (crystal violet, brilliant green), the azo (congo red) family, and unknown dyes in industrial wastewater, without the use of any radiation, expensive catalyst, acid, alkali, or deliberate alteration in pH. In our process, the ferrite was recovered by magnetic separation, and further, it was investigated for dye recovery.

A possible mechanism for the adsorption of dyes has been proposed based on our experimental results.

## 2. MATERIALS AND METHODS

**2.1. Materials.** Analytical-grade precursor oxide/carbonate powders were used for the synthesis of lithium-substituted magnesium ferrite. The precursor powders of iron(III) oxide, magnesium carbonate, and lithium carbonate in the mole ratio of 1:0.8:0.1 were ball-milled in acetone according to the stoichiometric formula  $\text{Mg}_{0.8}\text{Li}_{0.2}\text{Fe}_2\text{O}_4$  for 8 h. The obtained powder was calcined at 800 °C for 8 h, followed by pelletization into 1 × 1 square inch pellets. The calcined pellets were sintered at 970 °C for 4 h to obtain the final adsorbent material for dye removal. X-ray diffraction (XRD) of the synthesized sample was performed by a Rigaku P-E941 diffractometer using Cu K $\alpha$  radiation to determine the phase purity. The surface morphology and microstructure of the sample were analyzed by scanning electron microscopy (SEM) (Zeiss Evo MA-10). Photoluminescence spectroscopy (PL) was performed to detect the presence of oxygen-related defects with a photoluminescence spectrometer (Edinburgh Instruments, FLSP 900) at an excitation wavelength of 370 nm. Defects and the chemical environment of the elements in the synthesized ferrite were investigated by performing X-ray photoelectron spectroscopy at room temperature using an Al K $\alpha$  X-ray beam by the Scienta Omicron ultrahigh vacuum system as the excitation source. The Brunauer–Emmett–Teller (BET) surface area and pore size distribution of Li-MgF were quantified using nitrogen adsorption data obtained using the Quanta Chrome instrument (NOVA 2000e). The charge on the surface of the finely powdered sample in water as a dispersion medium was determined by performing  $\zeta$ -potential measurements on Zetasizer-Dynamic Light Scattering (M/s Malvern Instruments, U.K.). To investigate the magnetic characteristics of the adsorbent, a magnetic hysteresis loop was used with a vibrating sample magnetometer (Lakeshore 7304). High-purity brilliant green, congo red, and crystal violet dyes were procured from CDH. All of the solutions were prepared in Ultrapure Milli-Q water.

**2.2. Experimental and Analytical Procedure.** Textile industry wastewater was collected from a textile dyeing plant; 10 mL of each textile effluent was treated with 2 g of Li-MgF at the same pH at which it was received. The pH of the samples was measured using Eutech pH 700 m. To investigate the adsorption mechanism, a standard solution of 25 mM was prepared for three known dyes, brilliant green, crystal violet, and congo red, in Millipore water, and it was used throughout the study as the stock solution. Working solutions of 250, 200, 150, 100, and 50  $\mu\text{M}$  were prepared by the dilution method from the stock solution. Simultaneously, an artificial mixture of the dyes of an amount of 100  $\mu\text{M}$  each was also prepared to test the adsorption capability in a dye mixture. For the dye removal studies, 10 mL of the dye solution at each concentration was treated with 2 g of the Li-MgF in a vial. Intermediate shaking of the vials was performed to ensure proper contact of the dye molecules with the adsorbent at room temperature. Dye solutions with no adsorbent were used as control samples. The removal of dye from the solution was continuously monitored by performing UV–visible spectroscopy on a Shimadzu UV-1800 spectrophotometer at regular intervals. After 48 h, the Li-MgF was recovered from the solution. The total organic carbon (TOC) of the control and treated dye solution was performed with a Shimadzu TOC L

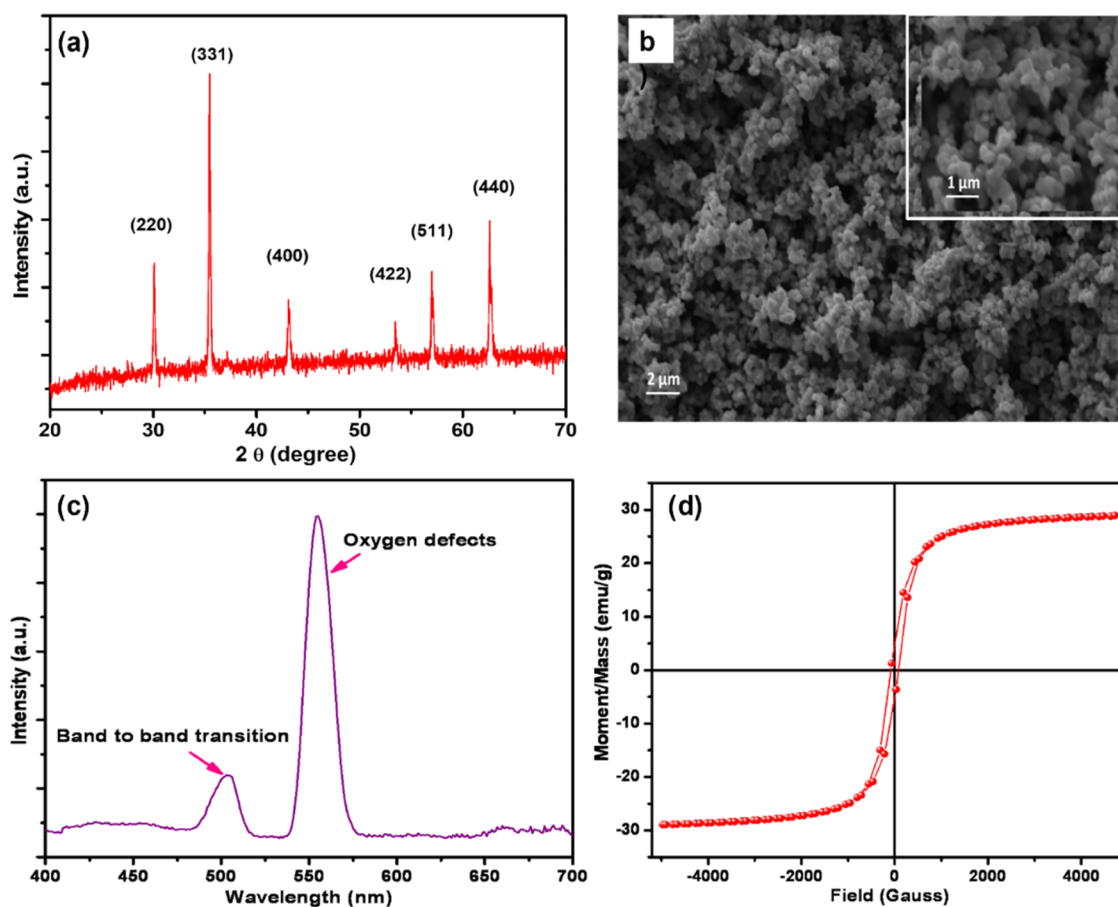


**Figure 1.** (a) XRD spectra of the synthesized Li-magnesium ferrite; (b) Li-MgF scanning electron micrograph; (c) Photoluminescence spectra of Li-MgF; and (d) magnetic moment of Li-MgF with respect to the applied magnetic field.

CPH/CPN analyzer to determine the total organic carbon before and after the treatment of the dye solutions. FTIR spectra of the adsorbent were recorded in the 400–3600  $\text{cm}^{-1}$  range before and after the dye adsorption process by mixing the finely powdered Li-MgF and freshly dehydrated KBr at a ratio of 1:50, and they were pressed into pellets. All experiments were performed without any alteration in the pH of the solution. However, the pH of water, when supplemented with Li-MgF, naturally reaches 8 to 10 because of the splitting of water molecules in the physisorbed layers by a high electric field generated in the nanopores of the material. The adsorption capacity  $q_e$  ( $\mu\text{mol/g}$ ) at equilibrium and the removal efficiency of the adsorbent were calculated as follows:

$$q_e = (C_0 - C_e)V/m \quad (1)$$

$$\% \text{ removal efficiency} = (C_0 - C_e) \times \frac{100}{C_0} \quad (2)$$

where  $C_0$  and  $C_e$  are the initial and equilibrium concentrations of the dye solution, respectively.  $V$  is the volume of dye solution in liters, and  $m$  is the mass of the adsorbent in grams.

Kinetic modeling of the adsorption of dyes on Li-MgF was performed by adopting four models as follows:

- (1) Pseudo-first-order adsorption model: This model assumes that the rate of adsorption depends on the concentration of a single component that is present in excess and indicates physical interaction/physorption as the dominant phenomenon and thus the rate-limiting

step. The equilibrium condition for the pseudo-first-order kinetics is represented by  $q_t = q_e [1 - e^{-k_1 t}]$ , where  $q_t$  and  $q_e$  are the adsorption capacities ( $\mu\text{mol/g}$ ) at equilibrium and time  $t$ , respectively.  $k_1$  is the rate constant for the pseudo-first-order reaction.

- (2) Pseudo-second-order adsorption model: This model assumes that the adsorption is driven by some physicochemical processes and depends on the adsorption sites available on the adsorbent surface. Here, the adsorption capacity of the adsorbent is the rate-limiting step. The pseudo-second-order adsorption process at time  $t$  is given by the expression  $\frac{t}{q_t} = \frac{1}{k_2 q_e^2} + \left(\frac{1}{q_e}\right)t$ , where  $k_2$  is a pseudo-second-order rate constant.

- (3) Elovich Model: This model provides more insights into the nature of chemisorption. The model is expressed by the equation  $q_t = \frac{1}{\beta} \ln(\alpha\beta) + \frac{1}{\beta} \ln t$ , where  $\alpha$  is the initial adsorption rate, and  $\beta$  is the desorption constant.

- (4) Intraparticle diffusion model: This model examines whether the adsorption of the adsorbate is driven by the surface or pore diffusion and is expressed by the equation  $q_t = K_p \sqrt{t} + C$ , where  $K_p$  is the rate constant, and  $C$  is the boundary layer thickness.<sup>33</sup>

Kinetic modeling was performed for the experimental data obtained at a concentration of 250  $\mu\text{M}$ . Further, to identify the type of interaction between the adsorbent and the adsorbate,

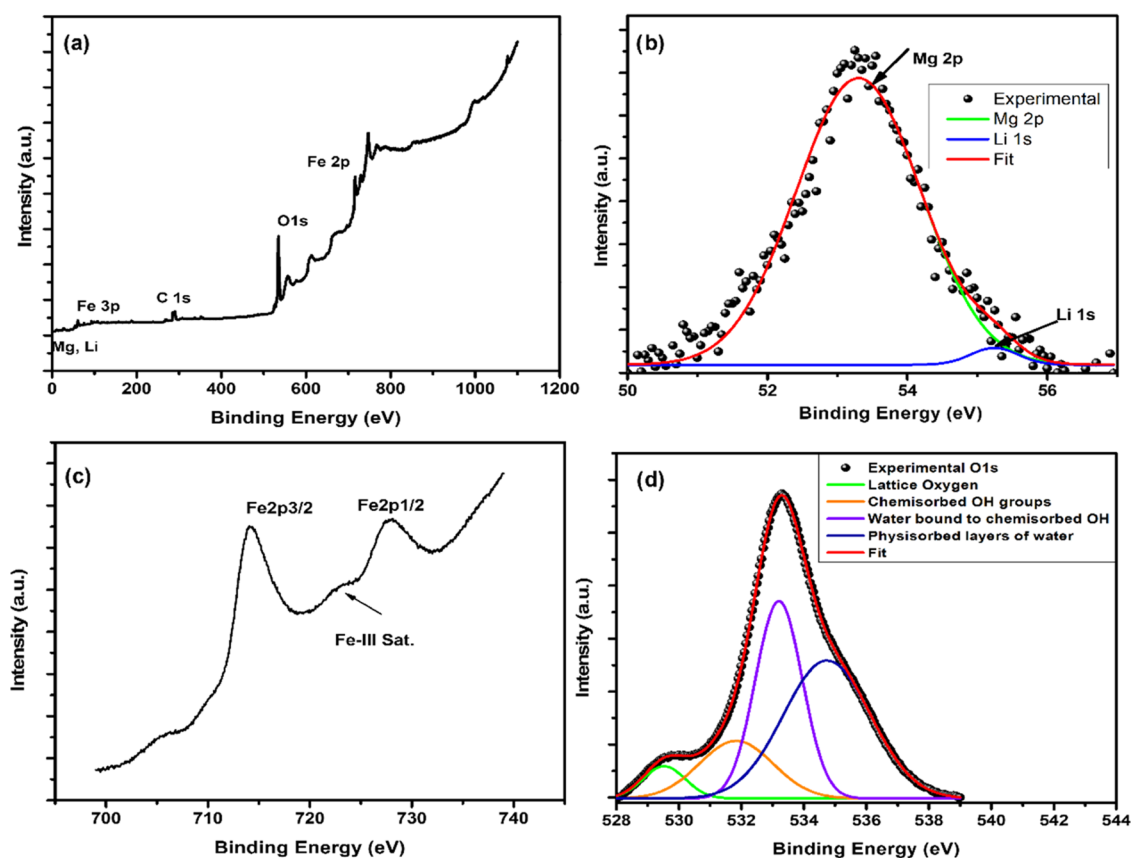


**Figure 2.** XPS (a) survey spectrum, (b) Mg 2p and Li 1s, (c) Fe 2p, and (d) O 1s.

the Langmuir, Freundlich, and Sips models were explored to fit the experimental adsorption isotherm data at equilibrium. The isotherm studies for all dyes were performed at room temperature i.e., 27 °C and at dye concentrations of 50, 100, 150, 200, and 250  $\mu\text{M}$ . For assessing the economic viability of the process, regeneration studies of the adsorbent were performed. Initially, 10 mL of methanol was added to the recovered adsorbent and extracted with continuous shaking for 2 h at room temperature. Then, the adsorbent was rinsed with water, followed by heat treatment at 500 °C. The recovered adsorbent was again used for dye adsorption, and the same process was repeated for up to three cycles.

### 3. RESULTS AND DISCUSSION

The X-ray diffraction of the synthesized Li-MgF pellet was performed to confirm the formation of a spinel structure (Figure 1a). No other impurity peaks were detected in the XRD spectra, confirming the formation of a pure spinel ferrite phase with the crystal planes (220), (331), (400), (422), (511), and (440) matching well with the JCPDS card no. 73-2211. The average crystallite size of the synthesized sample was calculated to be 26.6 nm with the XRD peak (331) using the Debye–Scherrer’s equation of  $D = k\lambda/\beta_{hkl} \cos \theta$ , where  $D$  is the average crystallite size,  $k$  is the shape factor (0.89),  $\lambda$  is the wavelength of Cu  $K\alpha$  radiation,  $\theta$  is the Bragg’s angle, and  $\beta_{hkl}$  is the full width at half-maximum of the diffraction peak.

Figure 1b exhibits a scanning electron micrograph of Li-MgF. A highly porous microstructure, along with irregularly shaped nanoparticles, is clearly visible in the image of the sintered Li-MgF. The nanoscale size and porous microstructure of the material expose a large surface area for the

maximum interaction with the dye to adsorb it rapidly from the dye effluent.<sup>34,35</sup> To gain insights into the surface defects, photoluminescence (PL) spectra were recorded with a laser excitation wavelength of 370 nm. The PL data revealed the presence of oxygen defects in the as-synthesized Li-MgF (Figure 1c). Two emission peaks were observed in the visible spectrum at 504 and 554 nm. The blue emission at 504 nm was assigned to band-to-band transitions in the material corresponding to a bandgap energy of 2.46 eV. The green emission at 554 nm was ascribed to the defect states within the band gap due to oxygen vacancies.<sup>36</sup> Oxygen vacancies are crucial defect centers that act as redox-active sites and promote the chemisorption of foreign molecules on the surface of a material.<sup>37,38</sup> Further, Wu et al. also demonstrated in their study that defective magnesium ferrite effectively removed the toxic arsenic(V) ions from contaminated water through the hydroxyl groups formed on the surface of the material in excess due to the presence of surface defects hydroxyl ions.<sup>39</sup> The substitution of magnesium by lithium atoms enhanced the oxygen vacancies in the synthesized Li-doped magnesium ferrite, and these oxygen vacancies in the material were found to be responsible for the dissociative adsorption of water molecules to generate green electricity by hydroelectric cells.<sup>28</sup> Hence, they can act as active agents for the adsorption of dye molecules from contaminated water. The magnetic character of the adsorbent helps in the easy separation of the adsorbent from the effluent or water bodies after treatment. Figure 1d exhibits the magnetization loop of the synthesized Li-MgF at room temperature. The saturation magnetization value obtained was 28.9 emu/g at an applied magnetic field of 5000 G. The coercivity value was obtained at 82.7 G, which

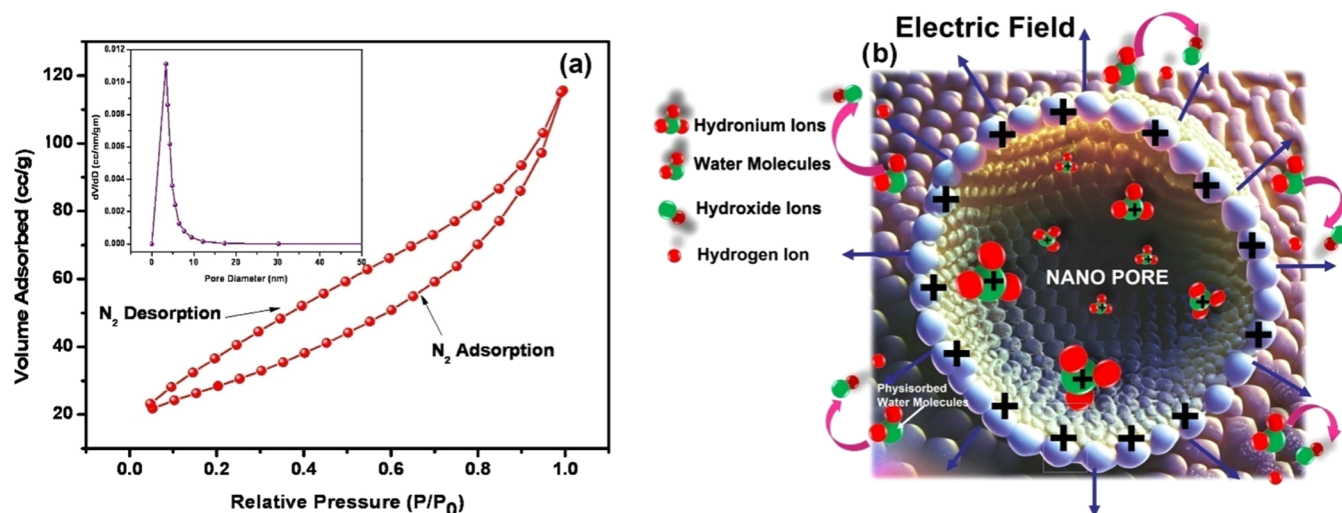


**Figure 3.** (a) BET surface area and pore volume distribution (inset). (b) Water physi-dissociation due to the electric field created in nanopores.

shows the soft magnetic character of the synthesized nanoferrite. Therefore, it can be easily recovered by magnetic separation after the adsorption of the pollutant.<sup>34</sup> X-ray photoelectron spectroscopy (XPS) was performed to characterize the chemical composition and oxidation state of the elements in the synthesized sample. The survey spectrum confirmed the presence of elements Li, Mg, Fe, and O in the sample (Figure 2a). All of the peaks were corrected for the charging factor with reference to the C 1s peak for adventitious carbon. Peak Fit software 4.2 was used to fit the obtained XPS peaks. The deconvoluted peaks centered at binding energies of 53.3 and 55.25 eV were attributed to Mg 2p and Li 1s, respectively. The core level XPS 2p peak positioned at 53.25 eV represents the magnesium in the ferrite lattice.<sup>40</sup>

The peak at 55.25 eV is attributed to the hydroxylated lithium/lithium oxide on the surface of the material (Figure 2b).<sup>41</sup> Two peaks located at 714 and 727.82 eV were associated with Fe 2p<sub>3/2</sub> and Fe 2p<sub>1/2</sub>, respectively, with a separation of 13.82 eV indicative of the presence of the Fe<sup>3+</sup> state of iron in the synthesized sample (Figure 2c).<sup>42</sup> The peak at 722.6 eV is a satellite peak characteristic of the core level XPS of Fe-III. The O 1s peak was deconvoluted into four peaks centered at 529.47, 531.79, 533.18, and 534.7 eV (Figure 2d). The peak at 529.47 eV was assigned to the lattice oxygen, while the peak at a binding energy of 531.92 was attributed to the chemisorbed layer of hydroxyl groups on the surface due to the chemi-dissociation of water near vacancy centers.<sup>43,44</sup> The peak centered at 533.18 eV was assigned to the water layer strongly bound to the chemisorbed hydroxyl monolayer. The peak centered at a high binding energy of ~534.7 eV was attributed to the strongly bound physisorbed water layers.<sup>45</sup> The presence of strongly bound water species on the environment exposed ferrite surface confirmed the highly reactive surface of the sample due to the presence of oxygen defects and nanopores deliberately created by the substitution of magnesium with lithium. Monovalent lithium substitution at divalent magnesium sites activated the removal of excess oxygen at high temperatures in the form of O<sub>2</sub> molecules to compensate for the charge. The insertion of two lithium ions creates one oxygen vacancy in the lattice according to the reaction  $\text{Li}_2\text{O} + \text{MgF} \rightarrow 2\text{Li}'_{\text{Mg}} + \text{O}_\text{o}^\times + \text{V}_\text{o}^{\bullet\bullet}$ .<sup>46</sup> Lithium doping disturbed the stoichiometry of the sample due to specific processing conditions.

Li-MgF displayed a type III adsorption–desorption isotherm according to the IUPAC convention. The BET surface area of the nanoporous material was determined to be 175 m<sup>2</sup>/g, with a wide distribution of pore sizes and an average pore diameter of 3.8 nm (Figure 3a). The high active surface area is one of the most important properties essential for effective adsorption. The small particle size also contributed to the reactivity of the sample surface, providing a large number of binding sites on the surface, as analyzed by BET. It helps enhance the adsorbent–adsorbate interaction and consequently a rapid adsorption process.<sup>47</sup> A large volume of nanopores is also beneficial, as it accelerates the dissociation of physisorbed water layers by creating a self-sustained high electric field inside the pores by trapping hydronium ions that accumulate a large concentration of hydroxide ions.

The mechanism of dissociation of water by nanopores is briefly illustrated in Figure 3b. Detailed calculations may be found in earlier studies.<sup>28</sup> When water approaches close to the nanoporous defective material, it gets chemi-dissociated on the material surface. There are multiple physisorbed water layers on the surface, and protons start hopping on the surface of physisorbed layers, popularly known as the Grothuss mechanism.<sup>48</sup> When these hopping protons get trapped inside a nanoconfined region due to the concentration of charge in the nanopores, a high electric field is created of the order of 10<sup>4</sup> V/cm.<sup>28</sup> This electric field is sufficient to dissociate water in the physisorbed layers. The protons are immediately trapped by available water or the material surface, leaving behind the OH<sup>−</sup> ions in the solution, which also contributes to an increase in the pH locally.

The surface charge of the adsorbent material plays a crucial role in determining the type and extent of interaction between the material and the dye. The ζ-potential on Li-MgF was found to be −11.5 mV, which confirmed the negative charge on ferrite particles in water (Figure S2). The negative charge is due to metal hydroxide formation on the ferrite surface, which is responsible for exerting the electrostatic force of attraction on the cationic dyes.<sup>49</sup>

**3.1. Adsorption of Textile Industry Wastewater.** The pH of the three effluents was measured using a benchtop pH meter before adsorption studies. The measured pH values were 7.0, 8.1, and 8.8 for the orange, blue, and brown samples, respectively. Figure 4a–c displays the UV–visible absorption

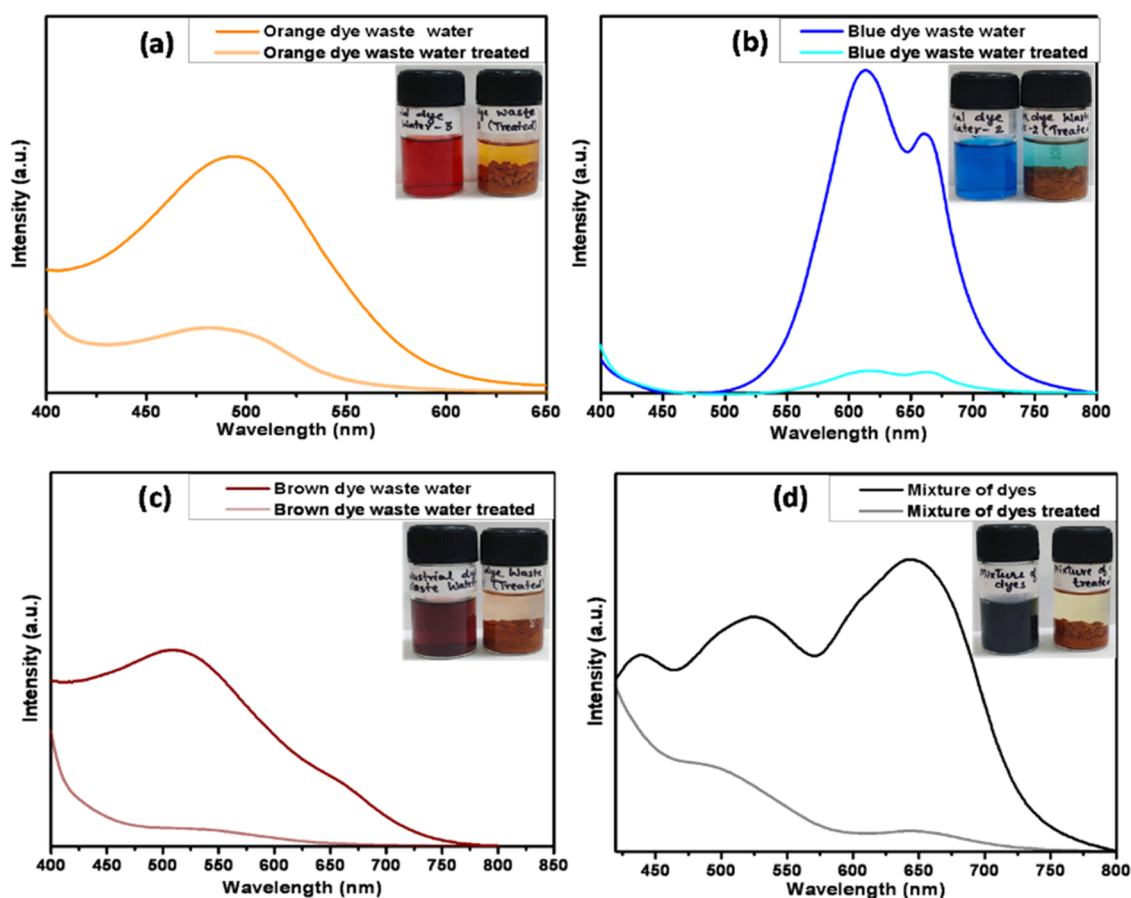


**Figure 4.** UV–visible spectra of unknown textile dyes contaminating wastewater before and after 48 h of treatment with (a–c) defective Li–MgF and (d) 100  $\mu\text{M}$  mixture of methylene blue, congo red, brilliant green, and crystal violet.

spectra of unknown dyes in textile wastewater and a mixture of known dye concentrations (Figure 4d) after 2 days of ferrite treatment. The orange textile dye showed broad absorption peak maxima at around 494 nm, and the blue textile dye at 613 nm with a shoulder at around 661 nm. The absorption peaks observed for the blue dye are characteristic of methylene blue; however, the shoulder found at around 613 nm became a peak indicating the existence of a significant dimeric form.<sup>50</sup> The brown textile dye showed the absorption maxima at around 512 nm, while the known dye mixture showed three prominent absorption peaks at 439, 524, and 644 nm, confirming the presence of multiple dyes. The adsorbent was able to decolorize the dye-contaminated wastewater completely or at least partially within 2 days. The UV absorption intensity of the orange dye decreased to 73%, while a more than 90% decrease in the UV absorption intensity was recorded for the brown dye, the blue dye, and the mixture of dyes. The known dye mixture became decolorized the same day within 6 h. A slight precipitation was observed in the mixture, which may be due to the presence of cationic as well as anionic dyes.

The presence of opposite charges led to attractive forces between dyes, and hence, their coprecipitation in the form of black suspended particles occurred. The treated known dye mixture was completely decolorized, which shows the enhanced synergistic removal of the dyes in a mixture. Li et al. also reported similar findings for a mixture of cationic and anionic dyes, for which they proposed a push and pull mechanism. The dimerized or trimerized dye molecule clusters already adsorbed on the adsorbent surface can act as effective

secondary sites to attract molecules of opposite charge. Hence, the enhanced removal of the coexisting dyes could be due to the multiple phenomena taking place simultaneously, for example, agglomeration due to the repulsion from the same type of charge, precipitation due to the interaction between opposite charges, and the availability of secondary sites (opposite charge) to easily adsorb on the adsorbent.<sup>49</sup>

**3.2. Dye Adsorption Measurements.** To investigate the mechanism of dye removal from the solution, UV–visible spectroscopy of the known dye solution was performed after regular intervals of 0, 2, 4, 6, 24, and 48 h, respectively, in the wavelength range of 200–800 nm. Figure 5a–c displays the UV–visible spectra of brilliant green (BG), crystal violet (CV), and congo red (CR) at 250  $\mu\text{M}$  concentration. The concentration of dyes in the solutions decreased with time, and the solution pH was measured at equilibrium for each dye. The pH values of the solutions of brilliant green, crystal violet, and congo red were measured to be 8.3, 8.3, and 8.1, respectively. Brilliant green showed the absorption maximum at 624 nm, with a sharp decrease in peak intensity within 2 h. Crystal violet shows the main absorption peak with a high-energy shoulder peak between 550 and 600 nm.<sup>51,52</sup> A sharp decrease in the intensity of the peak maxima after 2 h was observed. The interfacial interaction of crystal violet at the silica–water interface was measured in real time,<sup>53</sup> which suggested that CV can behave in the solution in two ways. First, it can be adsorbed on Li–MgF by electrostatic interactions due to the opposite polarity and removed from the solution. Second, it can undergo hydrolysis by the available

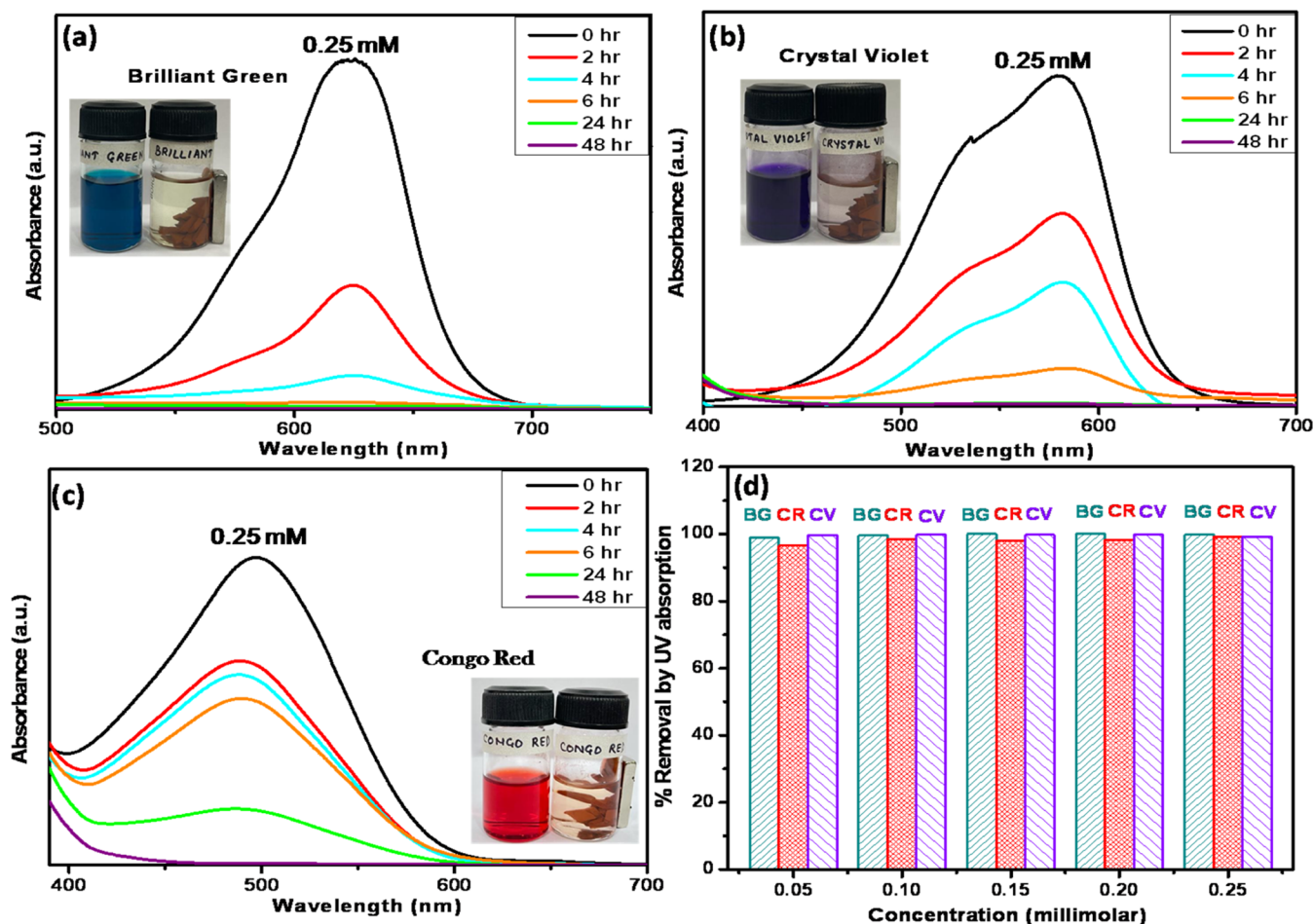


**Figure 5.** UV–visible spectra of (a) BG, (b) CV, and (c) CR. (d) Removal efficiency at varying concentrations.

OH<sup>-</sup> ions and get decolorized in the solution. The same phenomenon is also applicable to BG.<sup>54</sup> Congo red dye showed a slight different behavior. The maximum absorbance was observed at 497 nm, and a reduction in peak intensity with a small hypsochromic shift to 489 nm was evident in the UV–visible spectrum of congo red.

In the literature, studies on the blue shift during the adsorption process are rare. Kuan et al. observed a blue shift during the oxidative degradation of methylene blue by tunneled manganese oxide pyrolusite without using any radiation, where pyrolusite served as the oxidant.<sup>55</sup> The hypsochromic shift occurs because the polar adsorbent molecule reduces the energy of ground state n orbital by forming hydrogen bond.<sup>56</sup> Therefore, in the case of congo red, this may be due to amino group participation in the attachment to the polar heterogeneous surface of Li–MgF–OH through hydrogen bonding, leading to a hypsochromic shift of the maxima peak. Figure 5d depicts the effect of dye concentration on the removal efficiency of Li–MgF after 48 h. It is evident from the graph that the percentage removal of dye from the solution remained almost constant at all varying ranges of concentrations, indicative of the abundant adsorption sites and strong adsorbate–adsorbent interaction. The decolorization efficiency for all dyes ranged from 98 to 99%, except for congo red at 50  $\mu$ M, which was 96%.

The loading capacity plotted as a function of time is shown in Figure 6a–c for brilliant green, crystal violet, and congo red. Brilliant green and crystal violet reached equilibrium after 5–6

h of contact time with a sharp reduction in color intensity at all concentrations. The adsorption rate increased with an increase in the initial dye concentration for all dyes due to the decreased mass transfer resistance for dye molecules at higher concentrations.<sup>57</sup> However, congo red showed a slow adsorption process reaching equilibrium after 10–15 h, almost at all concentrations. Figure 6d exhibits the percent total organic carbon removal from the solution after 48 h at 250  $\mu$ M concentration. It is clearly visible that Li–MgF could effectively remove the organic carbon content from the solutions up to 46.46, 76.97, and 82.79% for crystal violet, congo red, and brilliant green, respectively. The TOC removal was comparatively low for CV, which further confirmed that some of the dye molecules remained in solution after hydrolysis; however, BG was removed from the solution to a large extent, which confirmed its adsorption on Li–MgF.

FTIR spectra of Li–MgF before and after the adsorption of the dyes congo red, crystal violet, and brilliant green are displayed in Figure 7a–d. In bare magnesium ferrite (Figure 7a), two characteristic peaks at 423 and 577  $\text{cm}^{-1}$  attributed to octahedral and tetrahedral metal–oxygen bond stretching in spinel ferrites are observed. The peaks at 1635 and 3451  $\text{cm}^{-1}$  were attributed to the –OH bending of water molecules and stretching vibrations of hydroxyls on ferrite, respectively, due to the adsorbed water molecules.<sup>58,59</sup> However, after dye adsorption, some other characteristic peaks ascribed to dye molecules appeared in the spectra, which confirmed the adsorption of dyes on Li–MgF. The peak in the range of 1400–

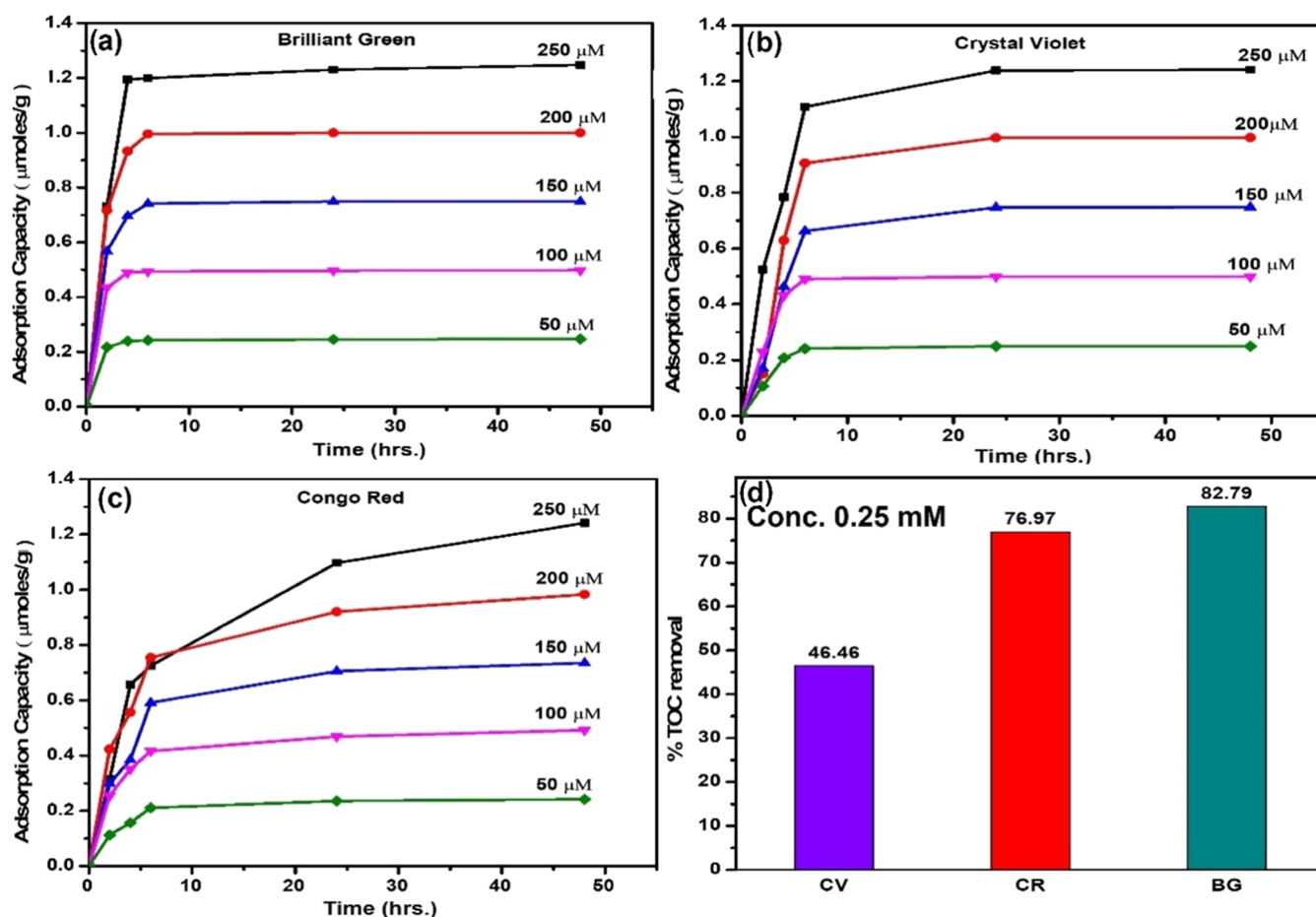


Figure 6. Variation of the adsorption capacity with time: (a) BG, (b) CV, (c) CR. (d) Total organic carbon removal after 48 h.

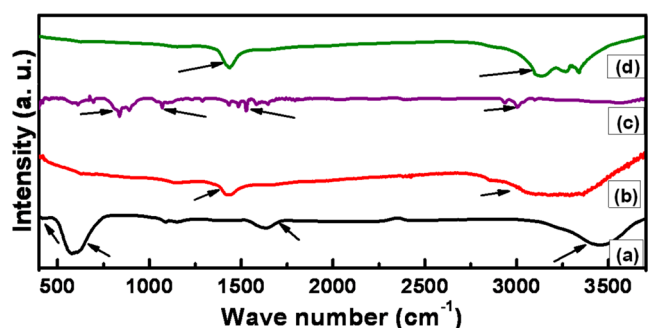


Figure 7. FTIR spectra of (a) bare Li-MgF, (b) CR-adsorbed Li-MgF, (c) CV-adsorbed Li-MgF, and (d) BG-adsorbed Li-MgF.

$1500\text{ cm}^{-1}$  is common to all dye adsorption spectra and corresponds to the C=C stretching of aromatic rings in the dye.<sup>60</sup> The other common peak for all dye-adsorbed samples was observed in the region between  $3000$  and  $3500\text{ cm}^{-1}$  ascribed to the =C–H stretching of aromatic rings and between  $3400$  and  $3500\text{ cm}^{-1}$  corresponding to overlapped N–H and O–H stretching. However, except for crystal violet, a slight shift toward lower frequencies is evident in the OH stretching peak, which may be due to the hydrogen bonding between dye molecules and hydroxyl groups on the ferrite surface.<sup>61</sup>

**3.3. Adsorption Kinetics of Dyes on Li-MgF.** To understand the mechanism of decolorization of the dyes by Li-MgF, the experimental known dye adsorption values

obtained were theoretically fitted on the four models frequently used for adsorption studies. The experimental data were fitted in the respective equations of pseudo-first-order and pseudo-second-order kinetic models, along with the Elovich and intraparticle diffusion models. The correlation coefficient for the fitted value and obtained parameters are shown in Table S1, and the respective fitting curves are presented in Figure 8. From Table S1, it is evident that the adsorption of brilliant green and crystal violet on Li-MgF follows pseudo-first-order kinetics with  $r^2$  (coefficient of determination) values of 0.98401 and 0.98762, respectively.

Conformity to the pseudo-first-order kinetic model indicated that, most likely, the dye adsorbed by Van der Waals forces on Li-MgF. As both the dyes are cationic and the hydroxylated material surface is negatively charged, the  $\zeta$ -potential signifies electrostatic interaction among dye molecules and the adsorbent. The adsorption of cationic dyes on negatively charged particles, which is the most common phenomenon taking place during adsorption between ionic species, has been well studied by many researchers.<sup>62,63</sup> It is important to note that TOC removal for brilliant green was around 83%, which indicated that Li-MgF was effective not only in the decolorization of the dye but also in removing the dye from the solution. However, crystal violet showed TOC removal up to 46.46%, which signifies that in addition to adsorption on the material, crystal violet decolorized in the solution. It is well reported in the literature that triarylmethane dyes can easily react with the available  $\text{OH}^-$  ions at high pH values due to the electrophilic nature of central carbon atoms in these dyes.<sup>64</sup>

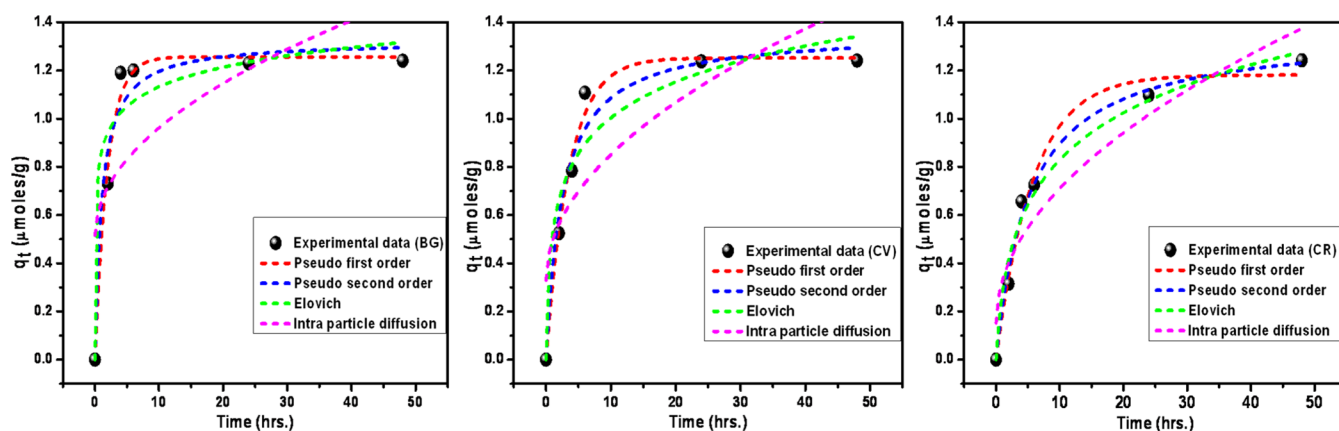


Figure 8. Theoretical kinetic model fitting for the obtained experimental values for BG, CV, and CR.

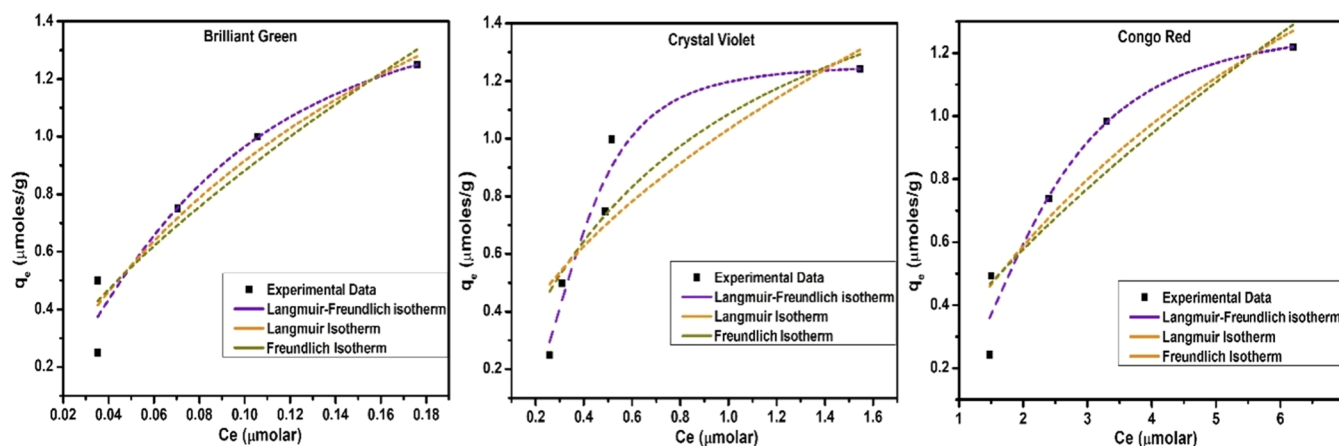


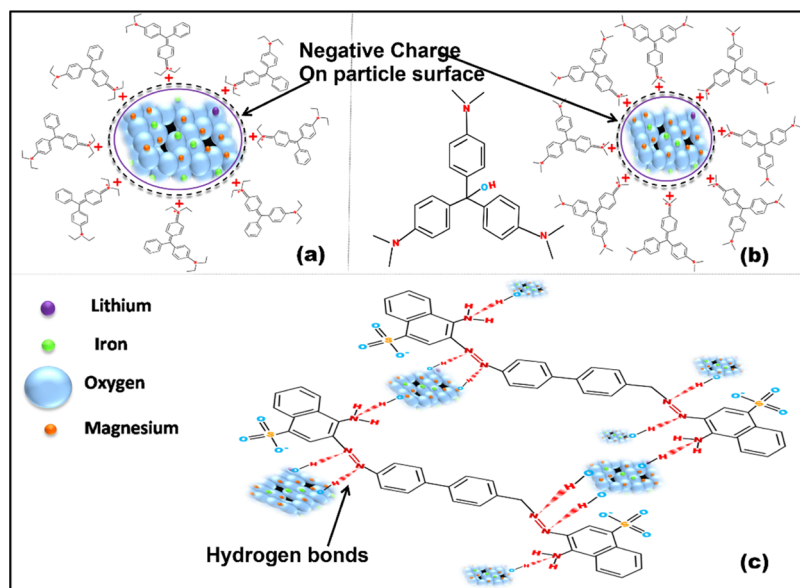
Figure 9. Isotherm nonlinear regression: Langmuir, Freundlich, and Sips models for BG, CV, and CR.

Table 1. Fitted Isotherm Model Constants and Correlation Coefficient Values Obtained in Each Case for Adsorption on Li-MgF

dye	Langmuir isotherm model			Freundlich isotherm model			Langmuir–Freundlich isotherm model			
	$Q_m$	$K_L$	$R^2$	$k_{Fr}$	$1/n$	$R^2$	$Q_{max}$	$K_s$	$n$	$R^2$
brilliant green	2.668	5.23	0.917	4.31	0.689	0.892	1.584	55.17	1.55	0.8998
crystal violet	1.99	1.196	0.76	1.03	0.544	0.68	1.259	19.077	3.048	0.91
Congo red	2.844	0.130	0.84	0.352	0.712	0.8	1.296	0.139	2.601	0.905

Their central carbon atom reacts with the  $\text{OH}^-$  ion and undergoes hydrolysis, which disrupts its conjugation. It may be possible that the  $\text{OH}^-$  ions generated by the dissociation of water in solution and on the adsorbent surface hydrolyzed BG and CV, hence limiting the conjugation to the isolated benzene rings and resulting in the disappearance of the color. The FTIR results clearly indicated the adsorption of the dyes on the material surface. TOC results showed that brilliant green has been removed from the solution to a greater extent in comparison to crystal violet. This may be due to the presence of nitrogen-alkyl chains on all three benzene rings of crystal violet, making its center more nucleophilic and active toward  $\text{OH}^-$  ions, simultaneously restricting the easy approach of the dye molecules to the material surface. Brilliant green has an amino-alkyl group on two benzene rings, and therefore, the less nucleophilic nature of the central carbon and less hindrance in comparison to crystal violet leads to a more facile approach toward the adsorbent surface.

Congo red showed the best fit with the pseudo-second-order kinetic model, indicating that the adsorption kinetics of congo red on Li-MgF is controlled by the chemisorption process, with an  $r^2$  value of 0.98985 (Table S1). The absorbance vs time graph also indicated the slow initial adsorption of congo red; this may be due to the fact that it is an anionic dye and adsorbent particles are also negatively charged; therefore, the repulsive force may be a limiting factor while approaching closer to the adsorbent.<sup>49</sup> TOC analysis showed that most of the dye was removed from the solution, implying that the dye molecules were adsorbed on the material surface. The blue shift in the UV–visible spectra of the dye indicated an exchange of electrons between them. The dye molecules were attached to the material surface through strong hydrogen bonds between the amino groups on the dye and the hydrogen atom of the surface hydroxyl groups. The first layer of adsorbed molecules may act as secondary adsorption sites, leading to the stacking of molecules. This phenomenon was further supported by the high pH (pH 8.1) of the solution due



**Figure 10.** Proposed mechanism of adsorption on Li-MgF for (a) BG, (b) CV, and (c) CR.

to the dissociation of water molecules. FTIR spectra of Congo red also indicated the strong hydrogen bonding of Congo red with the surface of the material.<sup>65</sup>

**3.4. Adsorption Isotherm Studies.** For isotherm studies, the experimental data were fitted for the Langmuir, Freundlich, and Sips models (Figure 9). All of the parameters derived from the isotherm fitting are given in Table 1. The Langmuir model is a two-parameter model that assumes the monolayer adsorption of the adsorbate on the homogeneously distributed specific sites on the adsorbent surface.<sup>66</sup>

The Langmuir equation in a nonlinear form is given as  $Q_e = Q_{\max} \times K_L \times C_e / (1 + K_L \times C_e)$ , where  $Q_e$  is the adsorption capacity at equilibrium,  $Q_{\max}$  is the maximum theoretical adsorption capacity of the adsorbent,  $K_L$  is the Langmuir constant related to the adsorption equilibrium, and  $C_e$  is the equilibrium concentration of the dye in solution. On the other hand, the Freundlich model, which is also a two-parameter model, applies to monolayer as well as multilayer adsorption on a heterogeneous surface. The nonlinear form of the model is given by the expression  $Q_e = K_F \times C_e^{1/n}$ , where  $Q_e$  is the adsorption capacity at equilibrium,  $K_F$  is the Freundlich constant related to the adsorption affinity and maximum adsorption, and  $1/n$  is the heterogeneity factor, which describes the intensity of adsorption.<sup>67</sup> However, similar to the Freundlich model, a model was proposed by Sips, which is a three-parameter model and is a combination of the Langmuir and Freundlich models. This model was proposed to overcome the limitation associated with the Freundlich model at sufficiently high concentrations. The nonlinear form of the model is given by the expression  $q_e = (Q_{\max} K_s \times C_e^n) / (1 + K_s \times C_e^n)$ , where  $Q_{\max}$  is the theoretical maximum loading capacity, and  $K_s$  is the equilibrium constant.<sup>66</sup> From the fitting parameters, it was observed that the Sips model fits well for all dyes. Brilliant green showed a close fit to the Langmuir model, with the highest correlation coefficient ( $R^2$ ) value of 0.917. The Sips model was also relatively successful in describing the adsorption mechanism, with an  $R^2$  value of 0.8998. This shows that the adsorption process is accompanied by both homogeneous and heterogeneous sites on the adsorbent.<sup>69</sup> The role of defects in adsorbents is to increase

the affinity of the adsorption sites toward the pollutant and other gases and induce strong interactions between them.<sup>70,71</sup> Interestingly, the crystal violet and congo red adsorption isotherms fitted well with the Sips model, with  $n > 1$  confirming the heterogeneity on the ferrite surface with variable adsorption energy sites and cooperative interaction between the sorbate and the adsorbent site.<sup>68</sup>

Obviously, defective Li-MgF consists of various surface defects such as unsaturated metal cations, oxygen vacancies, and a varying distribution of metal cations in sublattice sites.<sup>39</sup> The maximum adsorption capacity for BG was found to be 2.668  $\mu\text{mol/g}$  from the Langmuir fitting parameters, while the adsorption capacities for CV and CR were calculated to be 1.259 and 1.295  $\mu\text{mol/g}$ , respectively, from the parameters obtained by the Sips model. The isotherm model, indicating cooperative sorption, further supports the findings discussed above that crystal violet was decolorized by two mechanisms: first, due to the electrostatic interaction with the ferrite surface, and second, by the attack of  $\text{OH}^-$  ions at the central carbon atom of the dye generated due to the electric field in nanopores. The proposed mechanism for the interaction of brilliant green, crystal violet, and Congo red is displayed in Figure 10.

Brilliant green and crystal violet being positively charged adsorbed on the surface of negatively charged Li-MgF-OH by electrostatic interaction, although the presence of  $\text{OH}^-$  ions in the solution also contributed to the disappearance of the color of the dyes. Congo red bound to the surface of Li-MgF preferably by hydrogen bonding through interactions between the hydrogen atoms of hydroxyl groups formed on the surface of the material due to water dissociation and the azo bonds of the dye and those between the oxygen atom of the hydroxyl group and the hydrogen atom of the amine in congo red. The presence of charge generated by the electric field in nanopores facilitated van der Waals interactions for the adsorption of various dyes by multiple mechanisms.<sup>72</sup>

**3.5. Adsorbent Regeneration Studies.** The adsorbent regeneration process and economy play major roles in the industrial-scale application of an adsorbent. For example, the high regeneration cost of the most versatile adsorbent activated

carbon restricts its application in the industry.<sup>73</sup> Therefore, adsorbent regeneration and its efficiencies were further explored to determine the economic and large-scale viability of the process. The recovered Li-MgF from known as well as industrial wastewater samples was extracted with 10 mL of methanol for dye recovery, and then, the adsorbent was washed with DI water, followed by heat treatment at 500 °C for 2 h. Dyes at 250 μM concentration and the industrial wastewater were again treated with the regenerated adsorbent. This regeneration process was repeated for up to three cycles. The adsorption efficiency of the regenerated Li-MgF after multiple cycles with respect to the original adsorbent was calculated by measuring the absorbance of the treated dye wastewater after 48 h as follows

efficiency % of regenerated adsorbant with respect to fresh

$$\text{sample} = 100 - \left[ \frac{A_{\text{Reg}} - A_{\text{Orig}}}{A_{\text{Orig}}} \right] \times 100$$

$A_{\text{Reg}}$  is the absorbance of the dye wastewater treated with the regenerated adsorbent, and  $A_{\text{Orig}}$  is the absorbance of the wastewater treated with a fresh sample while the primary efficiency of the adsorbent was considered 100%.

BG and CV were recoverable from the adsorbent by methanol extraction, while CR could not be recovered, possibly due to the strong chemical binding with the Li-MgF surface. All industrial dyes were also recoverable; however, the extent of percent recovery was not part of this study. The efficiencies of the regenerated adsorbent with respect to adsorption by the fresh sample for the 250 μM dye solutions and industrial dye wastewater are shown in Figures S4 and S5, respectively. The efficacy of regenerated Li-MgF decreased to 98% for BG and CV, while it decreased to 95% for CR at the end of the third cycle. The adsorption efficiency decreased to 79.12, 88.3, and 89.47%, respectively, for orange, blue, and brown industrial dye wastewater at the end of the third regenerative cycle. This decrease in the adsorption efficiency of industrial dyes may be due to the presence of other chemicals and salts in the wastewater adsorbed on the surface of the material, which could not be removed by heating at low temperatures. The encouraging results obtained for the regenerated adsorbent show the facile recovery by low-temperature treatment and indicate the industrial-scale viability of the adsorbent in an economical and sustainable way, which is the foremost requirement in today's scenario.

#### 4. CONCLUSIONS

The cleaning of textile industry wastewater has been carried out effectively by nonphotocatalytic treatment using oxygen-deficient nanoporous Li-MgF. It has been systematically explored for the removal of known hazardous dyes emanating from the effluents of the textile industry. The presence of defects on the nanoporous material provides surface hydroxyl groups, and the electric field produced by nanopores facilitates the van der Waal force of attraction between the adsorbate and dye molecules by producing OH<sup>-</sup> ions. The abundance of hydroxyl groups and hydroxide ions increases the adsorption/decolorization efficiency of the material toward a variety of hazardous dyes. The type of interaction between the dye and the adsorbent, its decolorization, and the percent removal depends on the structure and chemistry of the dye molecule. It was observed that the synthesized Li-MgF responded quickly

and efficiently toward cationic triarylmethane-type dyes by electrostatic interaction as well as through OH<sup>-</sup> ion attack at the central carbon atom. This study showed that the oxygen defects and nanopores in Li-MgF activated the adsorption of cationic and anionic dyes. Li-MgF was found to be effective in decolorizing wastewater polluted with textile industry dye as well as a mixture of multiple known dyes with promising regeneration efficiency. The removal of the adsorbent (Li-MgF) is simple and easy with the use of a magnet. Thus, the use of the reusable, oxygen-deficient, ferromagnetic, nanoporous Li-MgF provides a highly scalable process to treat textile industry wastewater in an economical way to allow the reuse of the precious resource of water.

#### ■ ASSOCIATED CONTENT

##### SI Supporting Information

The Supporting Information is available free of charge at <https://pubs.acs.org/doi/10.1021/acsomega.3c09773>.

Images of commercial dye wastewater onsite sample collection, ζ-potential graph of the synthesized sample in water, table of kinetic constants and correlation coefficients obtained by the fitting of experimental data, table of isotherm constants and correlation coefficients obtained by fitting the experimental data, graphs obtained for adsorbent degeneracy up to three cycles with known dyes as well as unknown dyes (PDF)

#### ■ AUTHOR INFORMATION

##### Corresponding Author

Ravinder K. Kotnala – CSIR-National Physical Laboratory, Delhi 110012, India; [orcid.org/0000-0002-6570-4813](https://orcid.org/0000-0002-6570-4813); Email: [rkkotnala@gmail.com](mailto:rkkotnala@gmail.com)

##### Authors

Abha Shukla – Academy of Scientific and Innovative Research (AcSIR), Ghaziabad 201002 Uttar Pradesh, India; CSIR-National Physical Laboratory, Delhi 110012, India

Jyoti Shah – CSIR-National Physical Laboratory, Delhi 110012, India

Sunidhi Badola – Academy of Scientific and Innovative Research (AcSIR), Ghaziabad 201002 Uttar Pradesh, India; CSIR-National Physical Laboratory, Delhi 110012, India

Tuhin K. Mandal – CSIR-National Physical Laboratory, Delhi 110012, India

Ved V. Agrawal – CSIR-National Physical Laboratory, Delhi 110012, India; [orcid.org/0000-0002-5354-8833](https://orcid.org/0000-0002-5354-8833)

Asit Patra – CSIR-National Physical Laboratory, Delhi 110012, India

Lalsiemlien Pulamte – CSIR-National Institute of Science Communication and Policy Research, Delhi 110012, India

Complete contact information is available at:

<https://pubs.acs.org/doi/10.1021/acsomega.3c09773>

##### Notes

The authors declare no competing financial interest.

#### ■ ACKNOWLEDGMENTS

The authors are thankful to the Director of the National Physical Laboratory, Delhi, for the support and guidance. J.S. is thankful to the Department of Science & Technology for financial support.

## REFERENCES

- (1) Sabnis, R. W., Manufacture of Dye Intermediates, Dyes, and Their Industrial Applications. In *Handbook of Industrial Chemistry and Biotechnology*; Kent, J.; Bommaraju, T.; Barnicki, S., Eds.; Springer: Cham, 2017.
- (2) Benkhaya, S.; Mrabet, S.; Harfi, A. E. A Review On Classifications, Recent Synthesis And Applications Of Textile Dyes. *Inorg. Chem. Commun.* **2020**, *115*, No. 107891.
- (3) Al-Tohamy, R.; Ali, S.; Li, F.; Okasha, K. M.; Mahmoud, Y. A.-G.; Elsamahy, T.; Jiao, H.; Fu, Y.; Sun, J. A critical review on the treatment of dye-containing wastewater: Ecotoxicological and health concerns of textile dyes and possible remediation approaches for environmental safety. *Ecotoxicol. Environ. Saf.* **2022**, *231*, No. 113160.
- (4) Wang, X.; Jiang, J.; Gao, W. Reviewing textile wastewater produced by industries: characteristics, environmental impacts, and treatment strategies. *Water Sci. Technol.* **2022**, *85* (7), 2076–2096.
- (5) <https://www.europarl.europa.eu/news/en/headlines/society/20201208STO93327/the-impact-of-textile-production-and-waste-on-the-environment-infographics>.
- (6) Navin, P. K.; Kumar, S.; Mathur, M. Textile Wastewater Treatment: A Critical Review. *Int. J. Eng. Res. Technol.* **2018**, *6*, 1117.
- (7) Yaseen, D. A.; Scholz, M. Textile dye wastewater characteristics and constituents of synthetic effluents: a critical review. *Int. J. Environ. Sci. Technol.* **2019**, *16*, 1193–1226.
- (8) Berradi, M.; Hsissou, R.; Khudhair, M.; Assouag, M.; Cherkaoui, O.; Bachiri, A. E.; Harfi, A. E. Textile finishing dyes and their impact on aquatic environments. *Heliyon* **2019**, *5* (11), No. e02711.
- (9) Lellis, B.; Fávoro-Polonio, C. Z.; Pamphile, J. A.; Polonio, J. C. Effects of textile dyes on health and the environment and bioremediation potential of living organisms. *Biotechnol. Res. Innovation* **2019**, *3* (2), 275–290.
- (10) Gita, S.; Hussain, A.; Choudhury, T. G. Impact of textile dyes waste on aquatic environments and its treatment. *Environ. Ecol.* **2017**, *35* (3C), 2349–2353.
- (11) Brown, M. A.; De Vito, S. C. Predicting azo dye toxicity. *Crit. Rev. Environ. Sci. Technol.* **1993**, *23* (3), 249–324.
- (12) Azmi, W.; Sani, R. K.; Banerjee, U. C. Biodegradation of triphenylmethane dyes. *Enzyme Microb. Technol.* **1998**, *22* (3), 185–191.
- (13) Amines, S. A. *IARC Monographs on the Evaluation of Carcinogenic Risks to Humans*; IARC: 2018; p 99.
- (14) Ismail, M.; Akhtar, K.; Khan, M. I.; Kamal, T.; Khan, M. A.; Asiri, A. M.; Seo, J.; Khan, S. B. Pollution, toxicity and carcinogenicity of organic dyes and their catalytic bio-remediation. *Curr. Pharm. Des.* **2019**, *25* (34), 3645–3663.
- (15) Hussain, S.; Khan, N.; Gul, S.; Khan, S.; Khan, H. Contamination of Water Resources by Food Dyes and Its Removal Technologies. In *Water Chemistry*; IntechOpen: London, United Kingdom, 2019.
- (16) Ismail, M.; Akhtar, K.; Khan, M. I.; Kamal, T.; Khan, M. A.; Asiri, A. M.; Seo, J.; Khan, S. B. Pollution, Toxicity and Carcinogenicity of Organic Dyes and their Catalytic Bio-Remediation. *Curr. Pharm. Des.* **2019**, *25* (34), 3645–3663.
- (17) Hessel, C.; Allegra, C.; Maisseu, M.; Charbit, F.; Moulin, P. Guidelines and legislation for dye house effluents. *J. Environ. Manage.* **2007**, *83* (2), 171–180.
- (18) Grönwall, J.; Jonsson, A. C. Regulating effluents from india's textile sector: new commands and compliance monitoring for zero liquid discharge, 13/1 Law. *Environ. Dev. J.* **2017**, *13*, 15–29.
- (19) Ogugbue, C. J.; Sawidis, T. Bioremediation and Detoxification of Synthetic Wastewater Containing Triarylmethane Dyes by Aeromonas hydrophila Isolated from Industrial Effluent. *Biotechnol. Res. Int.* **2011**, *2011*, No. 967925, DOI: 10.4061/2011/967925.
- (20) Rane, A.; Joshi, S. J. Biodecolorization and Biodegradation of Dyes: A Review. *Open Biotechnol. J.* **2021**, *15* (1), 97–108.
- (21) Sarmah, K.; Pratihari, S. Synthesis, Characterization, and Photocatalytic Application of Iron Oxalate Capped Fe, Fe–Cu, Fe–Co, and Fe–Mn Oxide Nanomaterial. *ACS Sustainable Chem. Eng.* **2017**, *5*, 310–324.
- (22) Wang, W.; Lin, F.; Yan, B.; Cheng, Z.; Chen, G.; Kuang, M.; Yang, C.; Hou, L. The role of seashell wastes in TiO<sub>2</sub>/Seashell composites: Photocatalytic degradation of methylene blue dye under sunlight. *Environ. Res.* **2020**, *188*, No. 109831.
- (23) Albiss, B.; Abu-Dalo, M. Photocatalytic Degradation of Methylene Blue Using Zinc Oxide Nanorods Grown on Activated Carbon Fibers. *Sustainability* **2021**, *13*, 4729.
- (24) Vavilapalli, D. S.; Peri, R. G.; Sharma, R. K.; Goutam, U. K.; Muthuraaman, B.; Ramachandra Rao, M. S.; Singh, S. g-C<sub>3</sub>N<sub>4</sub>/Ca<sub>2</sub>Fe<sub>2</sub>O<sub>5</sub> heterostructures for enhanced photocatalytic degradation of organic effluents under sunlight. *Sci. Rep.* **2021**, *11*, No. 19639.
- (25) Ngomsik, A. F.; Bee, A.; Draye, M.; Cote, G.; Cabuil, V. Magnetic nano- and microparticles for metal removal and environmental applications: a review. *C. R. Chim.* **2005**, *8* (6–7), 963–970.
- (26) Ambashta, R. D.; Sillanpää, M. Water purification using magnetic assistance: A review. *J. Hazard. Mater.* **2010**, *180* (1–3), 38–49.
- (27) Li, Y.; Wang, T.; Zhang, S.; Zhang, Y.; Yu, L.; Liu, R. Adsorption and electrochemical behavior investigation of methyl blue onto magnetic nickel-magnesium ferrites prepared via the rapid combustion process. *J. Alloys Compd.* **2021**, *885*, No. 160969.
- (28) Kotnala, R. K.; Shah, J. Green hydroelectrical energy source based on water dissociation by nanoporous ferrite. *Int. J. Energy Res.* **2016**, *40*, 1652–1661.
- (29) Shah, J.; Kotnala, R. K. Rapid green synthesis of ZnO nanoparticles using a hydroelectric cell without an electrolyte. *J. Phys. Chem. Solids* **2017**, *108*, 15–20.
- (30) Shah, J.; Jain, S.; Shukla, A.; Gupta, R.; Kotnala, R. K. A facile non-photocatalytic technique for hydrogen gas production by hydroelectric cell. *Int. J. Hydrogen Energy* **2017**, *42* (52), 30584–30590.
- (31) Liu, F.; Leung, Y. H.; Djurišić, A. B.; Ching, N. A. M.; Chan, W. K. Native Defects in ZnO: Effect on Dye Adsorption and Photocatalytic Degradation. *J. Phys. Chem. C* **2013**, *117*, 12218–12228.
- (32) Wang, K.; Li, C.; Liang, Y.; Han, T.; Huang, H.; Yang, Q.; Liu, D.; Zhong, C. Rational Construction of Defects in a Metal-Organic Framework for Highly Efficient Adsorption and Separation of Dyes. *Chem. Eng. J.* **2016**, *289*, 486–493.
- (33) Kajjumba, G. W.; Emik, S.; Öngen, A.; Aydın, H. K. Ö. S.; Edebali, S. Modelling of Adsorption Kinetic Processes – Errors, Theory and Application. In *Advanced Sorption Process Applications*; IntechOpen: London, 2018.
- (34) Iram, M.; Guo, C.; Guan, Y.; Ishfaq, A.; Liu, H. Adsorption and magnetic removal of neutral red dye from aqueous solution using Fe<sub>3</sub>O<sub>4</sub> hollow nanospheres. *J. Hazard. Mater.* **2010**, *181* (1–3), 1039–1050.
- (35) Zhao, Z.; Bai, C.; An, L.; Zhang, X.; Wang, F.; Huang, Y.; Qu, M.; Yu, Y. Biocompatible porous boron nitride nano/microrods with ultrafast selective adsorption for dyes. *J. Environ. Chem. Eng.* **2021**, *9* (1), No. 104797.
- (36) Becker, A.; Kirchberg, K.; Marschall, R. Magnesium Ferrite (MgFe<sub>2</sub>O<sub>4</sub>) Nanoparticles for Photocatalytic Antibiotics Degradation. *Z. Phys. Chem.* **2020**, *234* (4), 645–654.
- (37) Yu, K.; Lou, L. L.; Liu, S.; Zhou, W. Asymmetric Oxygen Vacancies: The intrinsic redox active sites in metal oxide catalysts. *Adv. Sci.* **2019**, *57* (2), No. 1901970, DOI: 10.1002/adv.201901970.
- (38) Pandey, J.; Sethi, A.; Uma, S.; Nagarajan, R. Catalytic application of oxygen vacancies induced by Bi<sup>3+</sup> incorporation in th<sub>2</sub> samples obtained by solution combustion synthesis. *ACS Omega* **2018**, *3* (7), 7171–7181.
- (39) Wu, C.; Tu, J.; Tian, C.; Geng, J.; Lin, Z.; Dang, Z. Defective magnesium ferrite nano-platelets for the adsorption of As(V): The role of surface hydroxyl groups. *Environ. Pollut.* **2018**, *235*, 11–19.
- (40) Mkwae, P. S.; Kortidis, I.; Kroon, R. E.; Leshabane, N.; Jozela, M.; Swart, H. C.; Nkosi, S. S. Insightful Acetone Gas Sensing behaviour of Ce substituted MgFe<sub>2</sub>O<sub>4</sub> spinel nano- Ferrites. *J. Mater. Res. Technol.* **2020**, *9* (6), 16252–16269.

- (41) Wood, K. N.; Teeter, G. XPS on Li-Battery-Related Compounds: Analysis of Inorganic SEI Phases and a Methodology for Charge Correction. *ACS Appl. Energy Mater.* **2018**, *1*, 4493–4504.
- (42) Bazhan, Z.; Ghodsi, F. E.; Mazloom, J. The surface wettability and improved electrochemical performance of nanostructured  $\text{CoFe}_3 - \text{xO}_4$  thin film. *Surf. Coat. Technol.* **2017**, *309*, 554–562.
- (43) Saini, S.; Yadav, K. L.; Shah, J.; Kotnala, R. K. Effect of  $\text{Li}^+$ ,  $\text{Mg}^{2+}$ , and  $\text{Al}^{3+}$  Substitution on the Performance of Nickel Ferrite-Based Hydroelectric Cells. *Energy Fuels* **2022**, *36* (13), 7121–7129.
- (44) Jiang, L.; Wang, J.; Wu, X.; Zhang, G. A Stable  $\text{Fe}_2\text{O}_3$ /Expanded Perlite Composite Catalyst for Degradation of Rhodamine B in Heterogeneous Photo-Fenton System. *Water Air Soil Pollut.* **2017**, *228*, 463.
- (45) Shah, J.; Jain, S.; Gahtori, B.; Sharma, C.; Kotnala, R. K. Water Splitting on the mesoporous surface and oxygen vacancies of iron oxide generates electricity by hydroelectric cell. *Mater. Chem. Phys.* **2021**, *258*, No. 123981.
- (46) Balint, I.; Aika, K. Defect chemistry of lithium-doped magnesium oxide. *J. Chem. Soc., Faraday Trans.* **1997**, *93*, 1797–1801.
- (47) Sabzehmeidani, M. M.; Mahnaee, S.; Ghaedi, M.; Heidari, H.; Roy, V. A. L. Carbon based materials: a review of adsorbents for inorganic and organic compounds. *Mater. Adv.* **2021**, *2*, 598–627.
- (48) Cukierman, S. E. E. Grothuss! and other unfinished stories. *Biochim. Biophys. Acta* **2006**, *1757* (8), 876–885.
- (49) Li, H.; Cao, X.; Zhang, C.; Yu, Q.; Zhao, Z.; Niu, X.; Sun, X.; Liu, Y.; Li, M.; Li, Z. Enhanced adsorptive removal of anionic and cationic dyes from single or mixed dye solutions using MOF PCN-222. *RSC Adv.* **2017**, *7*, 16273.
- (50) Fernández-Pérez, A.; Marbán, G. Visible Light Spectroscopic Analysis of Methylene Blue in Water; What Comes after Dimer? *ACS Omega* **2020**, *5* (46), 29801–29815.
- (51) Sissaoui, J.; Budkina, D. S.; Vauthey, Eric. Torsional Disorder, Symmetry Breaking, and the Crystal Violet Shoulder Controversy. *J. Phys. Chem. Lett.* **2023**, *14* (24), 5602–5606.
- (52) Lewis, L. M.; Indig, G. L. Solvent effects on the spectroscopic properties of triaryl methane dyes. *Dyes Pigm.* **2000**, *46* (3), 145–154.
- (53) Xiong, Y.; Chen, J.; Duan, M.; Fang, S. Real-time measurement of the crystal violet adsorption behavior and interaction process at the silica–aqueous interface by near-field evanescent wave. *Phys. Chem. Chem. Phys.* **2018**, *20*, 19208–19220.
- (54) Salahudeen, N.; Rasheed, A. A. Kinetics and thermodynamics of hydrolysis of crystal violet at ambient and below ambient temperatures. *Sci. Rep.* **2020**, *10*, No. 21929.
- (55) Kuan, W. H.; Chan, Y. C. pH-dependent mechanisms of methylene blue reacting with tunneled manganese oxide pyrolusite. *J. Hazard. Mater.* **2012**, *239–240*, 152–159.
- (56) Rauf, M. A.; Soliman, A. A.; Khatib, M. Solvent effect on the spectral properties of Neutral Red. *Chem. Cent. J.* **2008**, *2*, 19.
- (57) Doğan, M.; Alkan, M.; Demirbaş, O.; Özdemir, Y.; Özmetin, C. Adsorption Kinetics of Maxilon Blue GRL onto Sepiolite from Aqueous Solutions. *Chem. Eng. J.* **2006**, *124*, 89–101.
- (58) Liu, X.; An, S.; Wang, Y.; Yang, Q.; Zhang, L. Rapid selective separation and recovery of a specific target dye from mixture consisted of different dyes by magnetic Ca-ferrites nanoparticles. *Chem. Eng. J.* **2015**, *262*, 517–526.
- (59) Das, K. C.; Dhar, S. S. Remarkable catalytic degradation of malachite green by zinc supported on hydroxyapatite encapsulated magnesium ferrite ( $\text{Zn}/\text{HAP}/\text{MgFe}_2\text{O}_4$ ) magnetic novel nanocomposite. *J. Mater. Sci.* **2020**, *55* (11), 4592–4606, DOI: 10.1007/s10853-019-04294-x.
- (60) Alshehri, A. A.; Malik, M. A. Biogenic fabrication of ZnO nanoparticles using *Trigonella foenum-graecum* (Fenugreek) for proficient photocatalytic degradation of methylene blue under UV irradiation. *J. Mater. Sci.: Mater. Electron.* **2019**, *30*, 16156–16173.
- (61) Banerjee, S.; Chattopadhyaya, M. C. Adsorption characteristics for the removal of a toxic dye, tartrazine from aqueous solutions by a low cost agricultural by-product. *Arab. J. Chem.* **2017**, *10* (2), S1629–S1638.
- (62) Singh, M.; Dosanjh, H. S.; Singh, H. Surface modified spinel cobalt ferrite nanoparticles for cationic dye removal: Kinetics and thermodynamics studies. *J. Water Process Eng.* **2016**, *11*, 152–161.
- (63) Bayantong, A. R. B.; Shih, Y. J.; Ong, D. C.; Abarca, R. R. M.; Dong, C. D.; de Luna, M. D. G. Adsorptive removal of dye in wastewater by metal ferrite-enabled graphene oxide nanocomposites. *Chemosphere* **2021**, *274*, No. 129518.
- (64) Rao, C. V.; Giri, A. S.; Goud, V. V.; Golder, A. K. Studies on pH-dependent color variation and decomposition mechanism of Brilliant Green dye in Fenton reaction. *Int. J. Ind. Chem.* **2016**, *7*, 71–80.
- (65) Lafi, R.; Montasser, I.; Hafiane, A. Adsorption of congo red dye from aqueous solutions by prepared activated carbon with oxygen-containing functional groups and its regeneration. *Adsorpt. Sci. Technol.* **2019**, *37* (1–2), 160–181.
- (66) Langmuir, I. The constitution and fundamental properties of solids and liquids. part I. Solids. *J. Am. Chem. Soc.* **1916**, *38*, 2221–2295.
- (67) Freundlich, H. M. F. Over the Adsorption in Solution. *J. Phys. Chem. A* **1906**, *57*, 385–471.
- (68) Keren, Y.; Borisover, M.; Bukhanovsk, N. Sorption interactions of organic compounds with soils affected by agricultural olive mill wastewater. *Chemosphere* **2015**, *138*, 462–468.
- (69) Pandian, A. M. K.; Karthikeyan, C.; Rajasimman, M. Isotherm and kinetic studies on adsorption of malachite green using chemically synthesized silver nanoparticles. *Nanotechnol. Environ. Eng.* **2017**, *2*, 2.
- (70) Afshariazar, F.; Morsali, A.; Sorbara, S.; Padial, N. M.; Roldan-Molina, E.; Oltra, J. E.; Colombo, V.; Navarro, J. A. R. Impact of Pore Size and Defects on the Selective Adsorption of Acetylene in Alkyne-Functionalized Nickel(II)-Pyrazolate-Based MOFs. *Chem. – Eur. J.* **2021**, *27* (46), 11837–11844.
- (71) Iacomini, P.; Formalik, F.; Marreiros, J.; Shange, J.; Rogackab, J.; Mohmeyer, A.; Behrens, P.; Ameloot, R.; Kuchta, B.; Llewellyn, P. L. Role of structural defects in the adsorption and separation of C3 hydrocarbons in Zr-fumarate-MOF (MOF-801). *Chem. Mater.* **2019**, *31* (20), 8413–8423.
- (72) Rychtowski, P.; Tryba, B.; Skrzypka, A.; Felczak, P.; Sreńscek-Nazzal, J.; Wróbel, R. J.; Nishiguchi, H.; Toyoda, M. Role of the Hydroxyl Groups Coordinated to  $\text{TiO}_2$  Surface on the Photocatalytic Decomposition of Ethylene at Different Ambient Conditions. *Catalysts* **2022**, *12*, 386.
- (73) Momina; Shahadat, M.; Suzylawati, I. Regeneration performance of clay-based adsorbents for the removal of industrial dyes: a review. *RSC Adv.* **2018**, *8* (43), 24571–24587.